Nonlinear Control-oriented Modeling for Very Flexible Aircraft

Molong Duan*, Carlos E. S. Cesnik†, and Ilya V. Kolmanovsky‡
University of Michigan, Ann Arbor, Michigan, 48109, USA

Fabio Vetrano§
Airbus Operations S.A.S., Toulouse, France

A low-order model for control design of very flexible aircraft (VFA) that accounts for geometrical nonlinearities under large deformations is derived in this work. The low-order model uses strain-based modal amplitudes as the flexible states and body-fixed frame linear and angular velocities for the basic flight dynamics. The model is informed by a set of nonlinear functions with explicit physical interpretations, representing the nonlinear structural and aerodynamics properties of VFA. These nonlinear functions can be obtained from higher fidelity structural and aerodynamic models or experimental tests. In this work, these nonlinear functions are captured by a set of neural networks, which are trained based on the data generated using nonlinear static results from the University of Michigan's Nonlinear Aeroelastic Simulation Toolbox (UM/NAST) solver. The resulting nonlinear VFA model is verified against UM/NAST dynamic simulation results using a representative high-aspect-ratio-wing transport aircraft model.

I. Introduction

Future transport aircraft are expected to have increased structural flexibility due to the reliance on lightweight materials and high aspect-ratio wings to improve fuel consumption and emissions. The increased flexibility, however, poses challenges to the modeling and control of the aircraft. Unlike models of a rigid aircraft with six degrees of freedom (DOF), models of flexible aircraft typically have hundreds or thousands of states [1, 2]. The simplest approach to deal with the model flexibility in control design is to correct the aerodynamic coefficients (flex/rigid ratios) in the 6-DOF rigid aircraft model and, potentially, include additional notch filters at the critical lowest frequencies to suppress the aeroelastic modes [3]. This approach may lead to low-performance controllers [4] and does not effectively address issues such as encountered in flutter control [5, 6]. On the other hand, the use of high-order models for controller design is also challenging due to the large number of states [7, 8], most of which are not directly measurable. Such approaches often yield high-order controllers that require actuators with unrealistically high performance/bandwidth for flexible aircraft [9]. Therefore, low-order flexible aircraft models that capture the nonlinear aeroelastic behavior are needed for controller design.

Such low-order models can be obtained by applying numerical model order reduction techniques to high-order models [7, 10, 11]. While well-developed procedures exist for linear model order reduction, effective and scalable nonlinear model order reduction is presently lacking. Furthermore, the physical meaning of the states and coefficients, which can be beneficial in the controller and observer design process, is typically lost when applying such procedures.

An alternative approach exploits the augmentation of additional aeroelastic terms to the conventional 6-DOF rigid aircraft model, leading to low-order analytical or semi-analytical nonlinear models [9]. This approach preserves the physical meaning of the states and various terms in the model.

Early investigations of this semi-analytical low-order flexible aircraft model exploited the concept of mean axes, and established the equations of motion using the instantaneous center of mass of the flexible aircraft as the reference point [5, 12, 13]. The mean axes formulation decouples the structural dynamics from the term describing the translational and rotational motions of the reference frame. A complementary approach is to formulate the problem based on a body frame with its origin fixed at a given point of the flexible aircraft [9, 14–16]. The model using body-fixed axes does not require small motion from the elastic body and, therefore, can account for the effect of the elastic deformation on the first- and second-mass moments of inertia; it produces more accurate results as the elastic motions increase in

---

magnitude [17]. Much of the previous literature assumed linear elasticity in their structural dynamics, leading to models that are well suited for flexible aircraft. However, as the flexibility levels increase, those approaches cannot account for the geometrical nonlinearities present in the very flexible aircraft (VFA) dynamics.

To establish a low-order model for VFA that captures the geometrical nonlinearities, Da Ronch et al. [18] presented a nonlinear model order reduction technique based on Taylor series expansion of the nonlinear high-order flight dynamics. Gibson *et al.* [15] used the dihedral angle as the flexible state and formulated a simple model of longitudinal flight dynamics of a very flexible flying wing. Su and Cesnik [19] introduced a strain modal-based nonlinear approach to reduce the number of flexible states. However, the evaluation of aerodynamics terms in [19] still requires the integration of the strains into generalized displacements, which prevented significant reduction in the computational cost of the full-order solution. Palacios and Cea [20] presented a very promising nonlinear modal condensation to Hodges' intrinsic beam theory to create the structural reduced-order model for a free-flying aircraft; however, no discussions were presented on the aerodynamic reduced-order model to go along with it.

This paper presents a new method to incrementally build a VFA low-order model combining the conventional 6-DOF rigid aircraft model, nonlinear structural dynamics, and data-driven low-order aerodynamics. The nonlinear functions are trained using neural networks and are based on the data generated from the full-order VFA model from the University of Michigan's Nonlinear Aeroelastic Simulation Toolbox (UM/NAST) [2]. The trained nonlinear functions are then used in the low-order dynamic simulations. The new low-order semi-analytical VFA model is exemplified using a representative high-aspect-ratio wing commercial transport aircraft as the VFA model.

This paper is organized as follows: The equations of motion of VFA and its derivation are summarized in Section II. Section III addresses the structural and aerodynamics nonlinear functions and formula to generate those terms from full-order UM/NAST models. In Section IV, a high-order UM/NAST model of the high-aspect-ratio-wing commercial transport aircraft as the VFA example is described. From it, nonlinear functions in the new low-order model are trained. The new low-order model is evaluated under longitudinal and lateral excitations, comparing its dynamic responses to the full-order UM/NAST dynamic solutions. Conclusions and future work are discussed in Section V.

II. Low-Order Model of Very Flexible Aircraft

A. Body-Fixed Axes Definition

Consider a VFA with a total mass of m. An inertial frame $\mathcal{F}_I$ with origin O_I and a body-fixed frame $\mathcal{F}_B$ with origin O_B (arbitrary point, but usually set as the aircraft undeformed center of mass) are defined as illustrated in Figure 1. The frame $\mathcal{F}_B$ is chosen to conform to the North-East-Down (NED) flight mechanics orientation and is related to frame $\mathcal{F}_I$ by a 3-2-1 Euler angle rotation (defined with Euler angles ϕ, θ, and ψ, respectively). The rotation matrix T_{IB} is defined as

$$T_{IB} = \begin{bmatrix} c(\psi)c(\theta) & c(\psi)s(\phi)s(\theta) - c(\phi)s(\psi) & s(\phi)s(\psi) + c(\phi)c(\psi)s(\theta) \\ c(\theta)s(\psi) & c(\phi)c(\psi) + s(\phi)s(\psi)s(\theta) & c(\phi)s(\psi)s(\theta) - c(\psi)s(\phi) \\ -s(\theta) & c(\theta)s(\phi) & c(\phi)c(\theta) \end{bmatrix}, \tag{1}$$

where $s(\cdot)$ and $c(\cdot)$ are short for $\sin(\cdot)$ and $\cos(\cdot)$ functions. The rotation matrix converts the coordinates in $\mathcal{F}_B$ to the ones in $\mathcal{F}_I$. For example, the velocity of the aircraft is defined as $\mathbf{V} = \frac{^I d}{dt}\mathbf{r}_{B/I}$, its representation in $\mathcal{F}_I$ (*i.e.*, $^I V$) and in $\mathcal{F}_B$ (*i.e.*, $^B V$) satisfy the following relationship

$$^I V = T_{IB}(^B V). \tag{2}$$

In this work, a vector projected into $\mathcal{F}_B$ frame is designated without extra notations, *e.g.*, $V = {}^B V$. The translational velocity (forward, lateral, and vertical speeds) and rotational velocity (roll, pitch, and yaw rates) of the aircraft in the body-fixed reference frame $\mathcal{F}_B$ are defined as $V = \{u, v, w\}^\top$ and $\omega = \{p, q, r\}^\top$, respectively. The orientation of $\mathcal{F}_B$ with respect to $\mathcal{F}_I$ is defined by roll-pitch-yaw Euler angles and the kinematics equations are given by

$$\frac{^I d}{dt} \left\{ \begin{array}{c} \phi \\ \theta \\ \psi \end{array} \right\} = \underbrace{\begin{bmatrix} 1 & \frac{s(\phi)s(\theta)}{c(\theta)} & \frac{c(\phi)s(\theta)}{c(\theta)} \\ 0 & c(\phi) & -s(\phi) \\ 0 & \frac{s(\phi)}{c(\theta)} & \frac{c(\phi)}{c(\theta)} \end{bmatrix}}_{R(\phi,\theta)} \left\{ \begin{array}{c} p \\ q \\ r \end{array} \right\}. \tag{3}$$
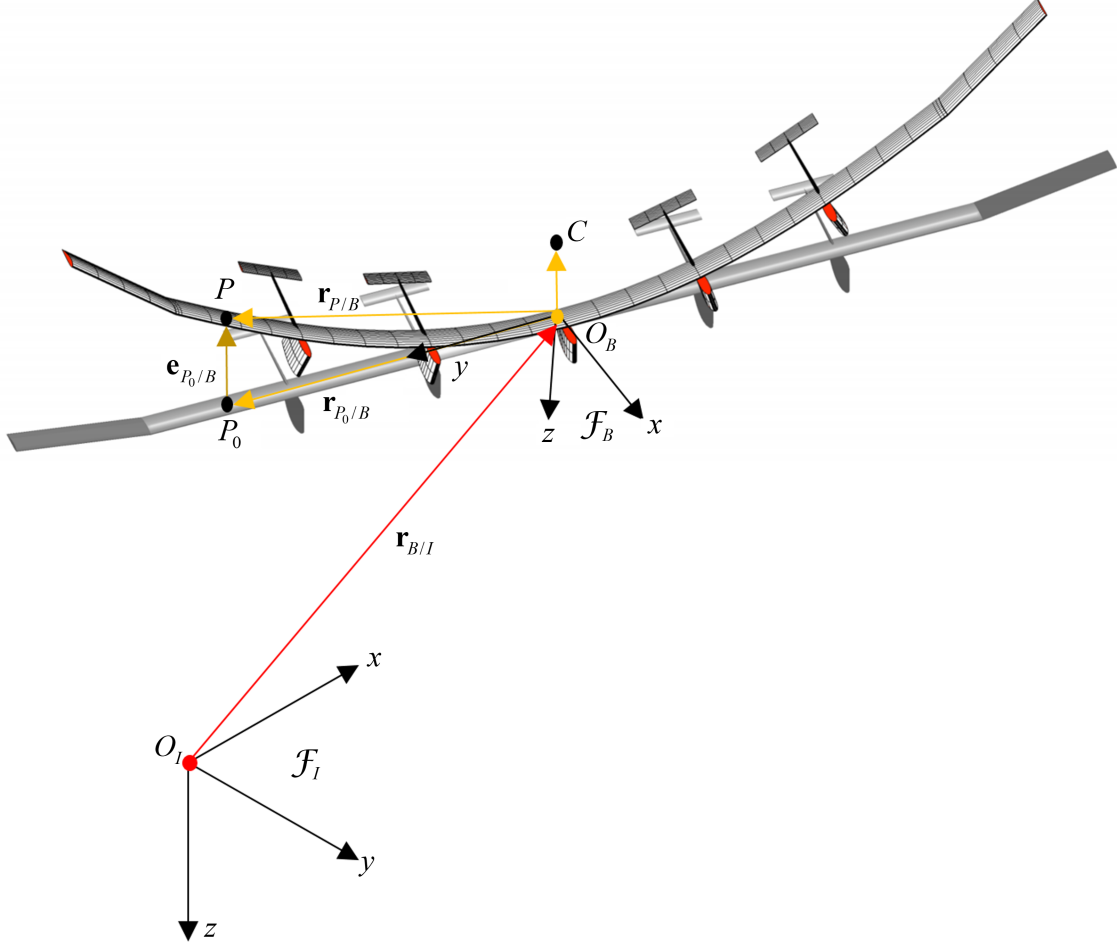
2

Fig. 1   Inertial and body-fixed axes of a very flexible aircraft

where $R(\phi, \theta)$ is the transformation matrix and ϕ, θ, and ψ are roll, pitch, yaw angles, respectively.

For an arbitrary point P on the aircraft, the vectors representing its position in reference frames $\mathcal{F}_I$ and $\mathcal{F}_B$ are written as $\mathbf{r}_{P/I}$ and $\mathbf{r}_{P/B}$, respectively. They satisfy the following relationship

$$\mathbf{r}_{P/I} = \mathbf{r}_{P/B} + \mathbf{r}_{B/I}, \tag{4}$$

where $\mathbf{r}_{B/I}$ is the inertial position of the vehicle (*i.e.*, relative to the origin O_I of $\mathcal{F}_I$). The time derivatives with respect to reference frames $\mathcal{F}_I$ and $\mathcal{F}_B$ are denoted by $\frac{^I d}{dt}$ and $\frac{^B d}{dt}$, respectively, and they are linked through the transport theorem as

$$\frac{^I d}{dt} V = \frac{^B d}{dt} V + \tilde{\omega} V, \tag{5}$$

where $\tilde{\omega}$ is the skew-symmetric matrix given by

$$\tilde{\omega} = \begin{bmatrix} 0 & -r & q \\ r & 0 & -p \\ -q & p & 0 \end{bmatrix}, \tag{6}$$

which converts cross product to matrix multiplication. This skew-symmetric matrix satisfies the properties $\tilde{\omega}^\top = -\tilde{\omega}$ and $\tilde{\omega} V = -\tilde{V} \omega$. Due to the extensively used $\mathcal{F}_B$ in this work, $\dot{V}$ and $\ddot{V}$ are compact forms of $\frac{^B d}{dt} V$ and $\frac{^B d^2}{dt^2} V$ for simplicity.

B. Equations of Motion of Very Flexible Aircraft

For VFA, the geometric nonlinearity needs to be considered; thus, the deformation vector e_{P_0} cannot be directly expressed as a linear combination of mode shapes. Therefore, the position vector of an arbitrary point, r_P, on the VFA is decomposed into the undeformed position, r_{P_0}, and its corresponding nonlinear deformation, e_{P_0}, as

$$r_P = r_{P_0} + e_{P_0} \approx r_{P_0} + \varphi(\eta, P_0), \tag{7}$$

where $\eta \in \mathbb{R}^n$ is a vector of reduced-order flexible states while $\varphi(\eta, P_0)$ is a nonlinear function representing the nonlinear displacement due to deformation. Accordingly, the translation of the center of mass due to deformation is a nonlinear function of η

$$e_C(\eta) = \frac{1}{m} \int_{P_0 \in \Omega_0} \varphi(\eta, P_0) \, dm. \tag{8}$$

Note that $e_C(\eta)$ is a nonlinear function with n-dimensional input and 3-dimensional output. Define $r_C(\eta)$ to be the position vector of the deformed center of mass with respect to the origin of $\mathcal{F}_B$, which satisfies $\frac{\partial r_C(\eta)}{\partial \eta} = \frac{\partial e_C(\eta)}{\partial \eta}$.

The equation of motion of a point mass m_P in reference frame $\mathcal{F}_B$ is given by [21]

$$m_P \left(\frac{{}^I d^2}{dt^2} r_{B/I} + \ddot{r}_P + \tilde{\dot{\omega}} r_P + 2\tilde{\omega}\dot{r}_P + \tilde{\omega}^2 r_P \right) = F_P, \tag{9}$$

where F_P is the total external force applied to the point mass. Note that the terms in Eq. (9) have explicit physical meanings: the first term on the left is the inertial force due to the moving frame $\mathcal{F}_B$; the second term is the inertial force of the point mass relative to the frame $\mathcal{F}_B$; the Euler, Coriolis, and Centripetal forces are the last three terms. The terms derived from this equation also follow this nomenclature and are denoted by *Frame*, *Relative*, *Euler*, *Coriolis*, and *Centripetal*, respectively. Direct integration of Eq. (9) and the integration with matrix product multiplier $\tilde{r}_P$ over the entire mass of the deformed aircraft yields the translational and rotational equations of motion (EOM) of the VFA, respectively. The EOMs for the reduced flexible states η are obtained through the principle of virtual work.

1. Translational Equations of Motion

The time derivatives of the nonlinear deformation function $\varphi(\eta, P_0)$ are given by

$$\begin{aligned}
\frac{{}^B d}{dt} \varphi(\eta, P_0) &= \varphi_\eta(\eta, P_0) \dot{\eta}, \\
\frac{{}^B d^2}{dt^2} \varphi(\eta, P_0) &= \frac{{}^B d}{dt} \left(\varphi_\eta(\eta, P_0) \dot{\eta} \right) = \dot{\eta}^\top \varphi_{\eta\eta}(\eta, P_0) \dot{\eta} + \varphi_\eta(\eta, P_0) \ddot{\eta},
\end{aligned} \tag{10}$$

where $\varphi_\eta(\eta, P_0)$ and $\varphi_{\eta\eta}(\eta, P_0)$ are the Jacobian and Hessian matrices, respectively. The translational EOM is written as

$$F_{\text{Frame}} + F_{\text{Relative}} + F_{\text{Euler}} + F_{\text{Coriolis}} + F_{\text{Centripetal}} = F_{\text{Ext}}, \tag{11}$$

where F_{Ext} is the vector of external forces applied to the VFA, while F_{Frame}, F_{Relative}, F_{Euler}, F_{Coriolis}, and $F_{\text{Centripetal}}$ are computed by integrating the corresponding terms in Eq. (9), *i.e.*,

$$F_{\text{Frame}} = \int_{P \in \Omega} \left(\frac{{}^I d^2}{dt^2} r_{B/I} \right) dm = m \frac{{}^I d}{dt} V = m \left(\dot{V} + \tilde{\omega} V \right), \tag{12}$$

$$\begin{aligned}
F_{\text{Relative}} &= \int_{P \in \Omega} \ddot{r}_P \, dm = \dot{\eta}^\top \left(\int_{P_0 \in \Omega_0} \varphi_{\eta\eta}(\eta, P_0) \, dm \right) \dot{\eta} + \left(\int_{P_0 \in \Omega_0} \varphi_\eta(\eta, P_0) \, dm \right) \ddot{\eta} \\
&= m\dot{\eta}^\top \frac{\partial^2 r_C(\eta)}{\partial \eta^2} \dot{\eta} + m \frac{\partial r_C(\eta)}{\partial \eta} \ddot{\eta},
\end{aligned} \tag{13}$$

$$F_{\text{Euler}} = \int_{P \in \Omega} \tilde{\dot{\omega}} r_P \, dm = -m\tilde{r}_C(\eta)\dot{\omega}, \tag{14}$$

4

$$F_{\text{Coriolis}} = \int\limits_{P \in \Omega} 2\tilde{\omega}\dot{r}_P \, dm = 2m\tilde{\omega}\frac{\partial r_C(\eta)}{\partial \eta}\dot{\eta}, \tag{15}$$

$$F_{\text{Centripetal}} = \int\limits_{P \in \Omega} \tilde{\omega}^2 r_P \, dm = m\tilde{\omega}^2 r_C(\eta). \tag{16}$$

The external force is decomposed into gravity, aerodynamics, and thrust terms as

$$F_{\text{ext}} = F_{\text{g}} + F_{\text{aero}} + F_{\text{thrust}}, \tag{17}$$

where $F_{\text{g}} = mg$ (g is the altitude-dependent gravitational acceleration vector projected into the body-fixed frame, $\mathcal{F}_B$) and

$$F_{\text{thrust}} = \sum_{i=1}^{n_{\text{T}}} T_i e_i(\eta), \tag{18}$$

where n_{T} is the number of thrust forces on the VFA, T_i is the thrust force provided by the ith thruster and e_i is the ith force pointing direction. For VFA, the thrust force's direction e_i is also a function of the flexible state, η. The aerodynamic force F_{aero} is assumed to be a nonlinear function of the rigid body velocities (*i.e.*, V, ω), flexible state and its rates (*i.e.*, η and $\dot{\eta}$), Euler angles (*i.e.*, ϕ, θ, and ψ), control surface deflections δ, and altitude h (due to the change of air density). The procedure to extract and train this nonlinear function is detailed in Section III.

2. Rotational Equations of Motion

The rotational EOM is derived by pre-multiplying both sides of Eq. (9) by $\tilde{r}_P$ and integrating, *i.e.*,

$$M_{\text{Frame}} + M_{\text{Relative}} + M_{\text{Euler}} + M_{\text{Coriolis}} + M_{\text{Centripetal}} = M_{\text{Ext}}, \tag{19}$$

where M_{Ext} is the external moment applied to the VFA with respect to the origin of $\mathcal{F}_B$. The terms M_{Frame} and M_{Relative} are given by

$$M_{\text{Frame}} = \int\limits_{P \in \Omega} \left(\tilde{r}_P \frac{{}^I d^2}{dt^2} r_{B/I}\right) dm = m\tilde{r}_C(\eta)\left(\dot{V} + \tilde{\omega}V\right), \tag{20}$$

and

$$\begin{aligned}
M_{\text{Relative}} &= \int\limits_{P \in \Omega} (\tilde{r}_P \ddot{r}_P) \, dm \\
&= \int\limits_{P_0 \in \Omega_0} \left(\tilde{r}_{P_0} + \tilde{\varphi}(\eta, P_0)\right)\left(\dot{\eta}^\top \varphi_{\eta\eta}(\eta, P_0)\dot{\eta} + \varphi_\eta(\eta, P_0)\ddot{\eta}\right) dm \\
&= \dot{\eta}^\top H_{\text{hess}}(\eta)\dot{\eta} + H_{\text{jac}}(\eta)\ddot{\eta},
\end{aligned} \tag{21}$$

where

$$\begin{aligned}
H_{\text{hess}}(\eta) &= \int\limits_{P_0 \in \Omega_0} \left(\tilde{r}_{P_0} + \tilde{\varphi}(\eta, P_0)\right)\varphi_{\eta\eta}(\eta, P_0) \, dm, \\
H_{\text{jac}}(\eta) &= \int\limits_{P_0 \in \Omega_0} \left(\tilde{r}_{P_0} + \tilde{\varphi}(\eta, P_0)\right)\varphi_\eta(\eta, P_0) \, dm.
\end{aligned} \tag{22}$$

The term M_{Euler} is given by

$$M_{\text{Euler}} = \int\limits_{P \in \Omega} \tilde{r}_P \tilde{\omega} r_P \, dm = I_B(\eta)\dot{\omega}, \tag{23}$$

where $I_B(\eta) = -\int\limits_{P \in \Omega} \tilde{r}_P \tilde{r}_P \, dm$ is the inertia matrix that can be further decomposed as

$$I_B(\eta) = -\int\limits_{P_0 \in \Omega_0} \left(\tilde{r}_{P_0} + \tilde{\varphi}(\eta, P_0)\right)\left(\tilde{r}_{P_0} + \tilde{\varphi}(\eta, P_0)\right) dm = I_B^{(0)} + I_B^{(1)}(\eta) + I_B^{(2)}(\eta), \tag{24}$$

5

where $I_B^{(0)} = - \int\limits_{P_0 \in \Omega_0} \left(\tilde{r}_{P_0} \tilde{r}_{P_0} \right) dm$ is the inertia matrix of the undeformed aircraft, and $I_B^{(1)}(\eta)$ and $I_B^{(2)}(\eta)$ are defined as

$$I_B^{(1)}(\eta) = - \int\limits_{P_0 \in \Omega_0} \left(\tilde{r}_{P_0} \tilde{\varphi}(\eta, P_0) + \tilde{\varphi}(\eta, P_0) \tilde{r}_{P_0} \right) dm,$$

$$I_B^{(2)}(\eta) = - \int\limits_{P_0 \in \Omega_0} \left(\tilde{\varphi}(\eta, P_0) \tilde{\varphi}(\eta, P_0) \right) dm. \tag{25}$$

The term M_{Coriolis} is given by

$$M_{\text{Coriolis}} = \int\limits_{P \in \Omega} 2 \tilde{r}_P \tilde{\omega} \dot{r}_P \, dm = 2 (J_0(\eta) \dot{\eta}) \omega, \tag{26}$$

where

$$J_0(\eta) = - \int\limits_{P_0 \in \Omega_0} \left(\tilde{r}_{P_0} + \tilde{\varphi}(\eta, P_0) \right) \tilde{\varphi}_\eta(\eta, P_0) \, dm. \tag{27}$$

The term $M_{\text{Centripetal}}$ is given by

$$M_{\text{Centripetal}} = \int\limits_{P \in \Omega} \tilde{r}_P \tilde{\omega} \tilde{\omega} r_P \, dm = \tilde{\omega} I_B(\eta) \, \omega. \tag{28}$$

This derivation exploits the property of cross product ($\tilde{u}_1 \tilde{u}_2 \tilde{u}_2 u_1 = -\tilde{u}_2 \tilde{u}_1 \tilde{u}_1 u_2$) for arbitrary vectors u_1 and u_2.

The external moment is decomposed into gravity, aerodynamics, and thrust terms as

$$M_{\text{ext}} = M_g + M_{\text{aero}} + M_{\text{thrust}}, \tag{29}$$

where

$$M_g = \int\limits_{P \in \Omega} (\tilde{r}_P g) dm = m \tilde{r}_C(\eta) g, \tag{30}$$

$$M_{\text{thrust}} = \sum_{i=1}^{n_T} T_i \tilde{r}_{\text{T},i}(\eta) e_i(\eta), \tag{31}$$

where $r_{\text{T},i}$ is the position of the ith thrust force. Similar to F_{aero}, the aerodynamic moment term M_{aero} is a nonlinear function of the rigid-body, flexible states, and control inputs, which is detailed in Section III.

3. The Equations of Motion of the Flexible States

One may proceed by computing the virtual work of various forces in Eq. (9) based on the virtual displacement $\delta\eta$. The corresponding virtual displacement at each point is specified by $\frac{\partial \varphi}{\partial \eta} \delta\eta$. As an expression of Hamilton's Principle, one has:

$$\delta U + \delta\eta^\top \left(\int\limits_{P \in \Omega} \frac{\partial \varphi}{\partial \eta}^\top \left(\frac{^I d^2}{dt^2} r_{B/I} + \ddot{r}_P + \tilde{\dot{\omega}} r_P + 2 \tilde{\omega} \dot{r}_P + \tilde{\omega}^2 r_P \right) dm - \int\limits_{P \in \Omega} \frac{\partial \varphi}{\partial \eta}^\top dF_P \right) = 0, \tag{32}$$

where U is the total potential energy of the deformable body that can be written as $\delta U = \delta\eta^\top Q_{\text{Elastic}}$ (more details in Section III). Accordingly, Eq. (32) is reduced to

$$Q_{\text{Elastic}} + Q_{\text{Frame}} + Q_{\text{Relative}} + Q_{\text{Euler}} + Q_{\text{Coriolis}} + Q_{\text{Centripetal}} = Q_{\text{Ext}}, \tag{33}$$

where

$$Q_{\text{Frame}} = \int\limits_{P \in \Omega} \left(\frac{\partial \varphi}{\partial \eta} \right)^\top \left(\frac{^I d^2}{dt^2} r_{B/I} \right) dm = m \left(\frac{\partial r_C(\eta)}{\partial \eta} \right)^\top (\dot{V} + \tilde{\omega} V), \tag{34}$$

$$Q_{\text{Relative}} = \int\limits_{P \in \Omega} \left(\frac{\partial \varphi}{\partial \eta} \right)^\top \ddot{r}_P \, dm = M(\eta) \ddot{\eta} + \frac{1}{2} \dot{\eta}^\top \frac{\partial M}{\partial \eta} \dot{\eta}, \tag{35}$$

6

where M_{ij} is the element of modal mass matrix M defined as

$$M_{ij} = \int_{P \in \Omega} \left(\frac{\partial \varphi}{\partial \eta_i} \right)^{\top} \left(\frac{\partial \varphi}{\partial \eta_j} \right) dm. \tag{36}$$

The Q_{Euler} is given by

$$Q_{\text{Euler}} = \int_{P \in \Omega} \left(\frac{\partial \varphi}{\partial \eta} \right)^{\top} \tilde{\omega} r_P dm = H_{\text{jac}}^{\top}(\eta) \dot{\omega}, \tag{37}$$

where $H_{\text{jac}}(\eta)$ is defined in Eq. (22). The term Q_{Coriolis} is written as

$$Q_{\text{Coriolis}} = \int_{P \in \Omega} 2 \left(\frac{\partial \varphi}{\partial \eta} \right)^{\top} \tilde{\omega} \dot{r}_P dm = 2 \left(\nu(\eta) \dot{\eta} \right) \omega, \tag{38}$$

where

$$\nu(\eta) = - \int_{P \in \Omega} \varphi_{\eta}^{\top} \tilde{\varphi}_{\eta} dm. \tag{39}$$

Note that the $H_{\text{jac}}(\eta)$ and $H_{\text{hess}}(\eta)$ defined in Eq. (22) satisfy following relationship

$$\frac{\partial H_{\text{jac}}(\eta)}{\partial \eta} = H_{\text{hess}}(\eta) + \int_{P \in \Omega} \tilde{\varphi}_{\eta} \varphi_{\eta} dm = H_{\text{hess}}(\eta) + \nu(\eta). \tag{40}$$

This relationship can be exploited in computations in that once $\nu(\eta)$ and $H_{\text{jac}}(\eta)$ are computed, $H_{\text{hess}}(\eta)$ is determined with $\frac{\partial H_{\text{jac}}(\eta)}{\partial \eta}$ and $\nu(\eta)$. The term $Q_{\text{Centripetal}}$ is defined as

$$Q_{\text{Centripetal}} = \int_{P \in \Omega} \left(\frac{\partial \varphi}{\partial \eta} \right)^{\top} \tilde{\omega}^2 r_P dm = -\omega^{\top} J_0(\eta) \omega, \tag{41}$$

where $J_0(\eta)$ is defined in Eq. (27). Assume strain-based deformation of η and the generalized elastic force is given by

$$Q_{\text{Elastic}} = \frac{\partial U}{\partial \eta} = K \eta. \tag{42}$$

The external generalized force $Q_{\text{Ext}} = \int_{P \in \Omega} \frac{\partial \varphi}{\partial \eta}^{\top} dF_P$ is decomposed into gravity, aerodynamics, and thrust terms as

$$Q_{\text{ext}} = Q_{\text{g}} + Q_{\text{aero}} + Q_{\text{thrust}}, \tag{43}$$

where

$$Q_{\text{g}} = \left(\frac{\partial r_C}{\partial \eta} \right)^{\top} g, \tag{44}$$

$$Q_{\text{thrust}} = \sum_{i=1}^{n_{\text{T}}} T_i \left(\frac{\partial \left(r_{\text{T},i}^{\top} e_i \right)}{\partial \eta} \right)^{\top}. \tag{45}$$

The aerodynamics term Q_{aero} is a nonlinear function of the rigid-body states, flexible states, and their rates, as well as the control surface deflections. The representation for Q_{aero} is derived by approximating the high-order nonlinear model as further detailed in Section III.

7

C. Summary of the Equations of Motion

Equations (11)-(45) are aggregated into a system of first-order ordinary differential equations that represent the evolution of rigid body and flexible states as

$$
E \frac{d}{dt} \begin{Bmatrix} V \\ \omega \\ \dot{\eta} \\ \eta \end{Bmatrix} = - \begin{Bmatrix} m\tilde{\omega}V + m\dot{\eta}^\top \frac{\partial^2 r_C(\eta)}{\partial \eta^2}\dot{\eta} + 2m\tilde{\omega}\frac{\partial r_C(\eta)}{\partial \eta}\dot{\eta} + m\tilde{\omega}^2 r_C(\eta) \\ m\tilde{r}_C(\eta)(\tilde{\omega}V) + \dot{\eta}^\top H_{\text{hess}}(\eta)\dot{\eta} + 2(J_0(\eta)\dot{\eta})\omega + \tilde{\omega}I_B(\eta)\omega \\ m\left(\frac{\partial r_C(\eta)}{\partial \eta}\right)^\top(\tilde{\omega}V) + \frac{1}{2}\dot{\eta}^\top\frac{\partial M}{\partial \eta}\dot{\eta} + 2(\nu(\eta)\dot{\eta})\omega - \omega^\top J_0(\eta)\omega + K\eta \\ -\dot{\eta} \end{Bmatrix} + \begin{Bmatrix} F_g + F_{\text{aero}} + F_{\text{thrust}} \\ M_g + M_{\text{aero}} + M_{\text{thrust}} \\ Q_g + Q_{\text{aero}} + Q_{\text{thrust}} \\ 0 \end{Bmatrix}, \quad (46)
$$

where

$$
E = \begin{bmatrix} m & -m\tilde{r}_C(\eta) & m\frac{\partial r_C(\eta)}{\partial \eta} & 0 \\ m\tilde{r}_C(\eta) & I_B(\eta) & H_{\text{jac}}(\eta) & 0 \\ m\left(\frac{\partial r_C(\eta)}{\partial \eta}\right)^\top & H_{\text{jac}}^\top(\eta) & M(\eta) & 0 \\ 0 & 0 & 0 & I_n \end{bmatrix}.
\quad (47)
$$

The equations of motion in Eq. (46), together with kinematics given in Eqs. (2) and (3), form a complete set of VFA equations of motion.

III. Nonlinear Functions Identification Exploiting Strain-based Full-order Models

The EOM in Eq. (46) contains a set of nonlinear functions, including aerodynamic forces and moments, that depend on the nonlinear structural deformation and they must be numerically obtained. These nonlinear terms and their input-output dimensions are specified in Table 1. For the structural terms, the vector of flexible states η is sufficient to represent the nonlinear deformation, and thus the input dimensions are relatively low. Some structural terms are symmetric (*e.g.*, I_B, M) or have fixed norm (*e.g.*, e_i). Considering these properties, the output dimensions of these terms are reduced. Note that we assume that the derivatives of the nonlinear functions can be directly computed. Therefore, as discussed in Section II.B.3, the term H_{hess} can be computed based on Eq. (40). The aerodynamic terms F_{aero}, M_{aero}, and Q_{aero} take the rigid body velocities (*i.e.*, V, ω), flexible states and their rates (*i.e.*, η and $\dot{\eta}$), Euler angles (*i.e.*, ϕ, θ, and ψ), control surface deflections δ, and altitude h as input. Therefore, the input dimension for the aerodynamic terms is $2n + n_\delta + 10$, where n_δ is the number of control surfaces.

Table 1   Identified nonlinear functions and their dimensions

	Nonlinear function	Input/output dimension
Structural terms	$r_C(\eta)$	$\mathbb{R}^n \to \mathbb{R}^3$
	$r_{\text{T},i}(\eta)$	$\mathbb{R}^n \to \mathbb{R}^3$
	$e_i(\eta)$	$\mathbb{R}^n \to \mathbb{R}^2$ (due to unit vector)
	$I_B(\eta)$	$\mathbb{R}^n \to \mathbb{R}^6$ (due to symmetry)
	$M(\eta)$	$\mathbb{R}^n \to \mathbb{R}^{n(n+1)/2}$ (due to symmetry)
	$H_{\text{jac}}(\eta)$	$\mathbb{R}^n \to \mathbb{R}^{3 \times n}$
	$J_0(\eta)$	$\mathbb{R}^n \to \mathbb{R}^{3 \times 3 \times n}$
	$\nu(\eta)$	$\mathbb{R}^n \to \mathbb{R}^{n \times 3 \times n}$
Aerodynamic terms	F_{aero}	$\mathbb{R}^{2n+n_\delta+10} \to \mathbb{R}^3$
	M_{aero}	$\mathbb{R}^{2n+n_\delta+10} \to \mathbb{R}^3$
	Q_{aero}	$\mathbb{R}^{2n+n_\delta+10} \to \mathbb{R}^n$

Although the selected flexible state η is designed to be a low-dimensional vector representing the main strain-based modes, the corresponding nonlinear functions are computed by the integration over the entire aircraft body, and hence require a high-fidelity description of the deformation. In this work, this high-fidelity deformation information and aerodynamics are extracted from UM/NAST [2], which adopts nonlinear beam elements and strain-based formulation. In the UM/NAST formulation [2], nonlinear beam elements are employed to model the elastic deformation of VFA.

Consider s as the curvilinear beam coordinate shown in Figure 2, and $h(s)$ describing the position and orientation of each node along the beam with a vector consisting of 12 components, *i.e.*,

$$h(s)^\top = \left\{ \begin{array}{cccc} [r_B + r_w(s)]^\top & w_x(s)^\top & w_y(s)^\top & w_z(s)^\top \end{array} \right\}, \tag{48}$$

where r_B is the column vector of the body position vector of the aircraft's body-fixed reference frame $\mathcal{F}_B$ origin, $r_w(s)$ is the column vector of the position vector of a node along the beam reference line with respect to the origin of $\mathcal{F}_B$, both expressed in the body-fixed frame. The column vectors $w_x(s)$, $w_y(s)$, $w_z(s)$ represent the unit vectors of a triad on the deformed beam frame pointing along the beam reference axis, towards the leading edge, and normal to beam surface, respectively, resolved in the body frame.
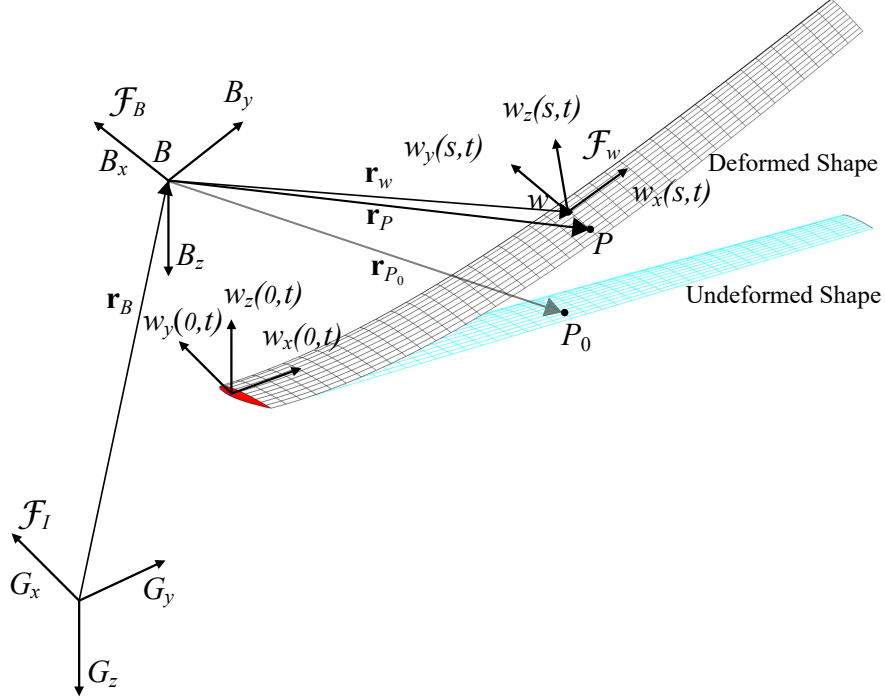
Fig. 2   UM/NAST coordinate systems and basic position/orientation vectors. The w_x, w_y and w_x are shown as functions of s.

Beam elements with constant strains are employed in UM/NAST to model the nonlinear deformation. Within each constant-strain element, the strain vector is given by

$$\epsilon_e^\top = \left\{ \begin{array}{cccc} \epsilon_x & \kappa_x & \kappa_y & \kappa_z \end{array} \right\}, \tag{49}$$

where ϵ_x is the extensional strain, κ_x, κ_y, and κ_z are the twist of the beam reference line, bending about the local w_y axis, and bending about the local w_z axis, respectively. The advantage of such selection is that the strain vector is a local variable associated with the element, which does not explicitly depend on the states of other elements. Accordingly, strain-based formulation allows to maintain a constant stiffness matrix without the assumption of small deformation, which is especially beneficial in the VFA modeling where large deformation and geometrical nonlinearity must be captured. The total strain vector of the complete aircraft is obtained by assembling the strain vector of all elements as

$$\epsilon^\top = \left\{ \begin{array}{cccc} \epsilon_{e1}^\top & \epsilon_{e2}^\top & \epsilon_{e3}^\top & \cdots \end{array} \right\}. \tag{50}$$

The UM/NAST solver [2] computes the displacement $h(\epsilon)$, the Jacobian matrix $J_{h\epsilon}(\epsilon) = \frac{\partial h}{\partial \epsilon}$, and mass terms (*e.g.*, $M_{BB}(\epsilon)$ and $M_{FF}(\epsilon)$) for given ϵ. It also computes the total aerodynamic forces F_{aero}, M_{aero}, and Q_{aero} with additional dependence on rigid-body states, control surface deflections, and strain rate states. Therefore, as shown in Figure 3,

UM/NAST can be used as a tool to generate the values of the nonlinear terms to be trained in Table 1 for a large number of random inputs within prescribed bounds. Note that the outputs of the UM/NAST need to be reformulated and calculated to get the derived nonlinear terms in Table 1; the process is detailed in this section. The processed input and output data are then fitted with neural networks, the analytical derivatives of which can be symbolically computed as described in the Appendix.
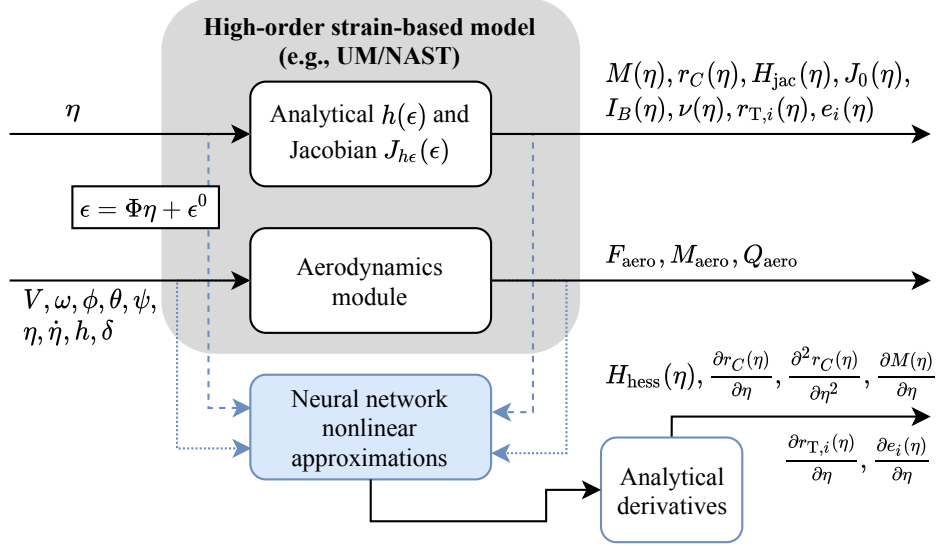

Fig. 3 UM/NAST model used for data generation for nonlinear function training in the low-order model

Now consider the strain-based modal amplitude η defined in Section II connected to the full strain state ϵ via

$$\epsilon = \Phi\eta + \epsilon^0, \tag{51}$$

where ϵ^0 is the initial strain state where the modal decomposition is performed about it. This ϵ^0 can be selected to be a trimmed strain state at a representative flight condition or any other initial state from which the dynamic motion of interest will evolve. The potential energy is written as

$$U = \frac{1}{2}\epsilon^\top K_\epsilon \epsilon. \tag{52}$$

Therefore, Q_{Elastic} in Eq. (42) is given by

$$Q_{\text{Elastic}} = K\eta + \Phi^\top K_\epsilon \epsilon^0. \tag{53}$$

where the generalized stiffness matrix is given by

$$K = \Phi^\top K_\epsilon \Phi. \tag{54}$$

The Jacobian matrix with respect to η is defined as

$$J_{h\eta} = J_{h\epsilon}\Phi. \tag{55}$$

In UM/NAST, the mass terms $M_{BB}(\epsilon)$ and $M_{FF}(\epsilon)$ are expressed as functions of ϵ. Using the expression

$$M_{BB} = \begin{bmatrix} mI_3 & -m\tilde{r}_C(\eta) \\ m\tilde{r}_C(\eta) & I_B(\eta) \end{bmatrix}, \tag{56}$$

the nonlinear terms $r_C(\eta)$ and $I_B(\eta)$ can be directly extracted. Similarly, the mass matrix for the flexible states $M(\eta)$ in the new formulation is computed following

$$M(\eta) = \Phi^\top M_{FF}\Phi. \tag{57}$$

Note that in the UM/NAST formulation, the position of an arbitrary point is established as

$$r_P = r_w + y w_y + z w_z, \tag{58}$$

where the pair (y, z) defines the position of a point within a local beam cross-section frame $\mathcal{F}_w$. Accordingly, the component of $H_{\text{jac}}(\eta)$ for a single element (defined as $H_{\text{jac}}^{(e)}(\eta)$) is given by

$$H_{\text{jac}}^{(e)}(\eta) = \int_{\Delta s} \int_{A(s)} (\tilde{r}_w + y \tilde{w}_y + z \tilde{w}_z) \left(\frac{\partial r_w}{\partial \eta} + y \frac{\partial w_y}{\partial \eta} + z \frac{\partial w_z}{\partial \eta} \right) \rho \, dA \, ds. \tag{59}$$

Define the cross-section inertia matrix $M^{\text{CS}}(s)$ and the element inertia matrix $M^{(e)}$ as [2]

$$M^{\text{CS}}(s) = \int_{A(s)} \rho \begin{bmatrix} 1 & 0 & y & z \\ 0 & 0 & 0 & 0 \\ y & 0 & y^2 & yz \\ z & 0 & zy & z^2 \end{bmatrix} dA, \tag{60}$$

$$M^{(e)} = \int_{\Delta s} M^{\text{CS}}(s) \, ds. \tag{61}$$

Also, r_w, w_x, w_y, and w_z for the eth element are components of the h vector, and are denoted as $h^{(e)}(1)$, $h^{(e)}(2)$, $h^{(e)}(3)$, and $h^{(e)}(4)$, respectively. Similar notation is also used for the segmentation of the Jacobian matrices $J_{h\epsilon}$ and $J_{h\eta}$. Note that $M^{(e)}$ is a part of the mass matrix provided by UM/NAST, while r_w, w_x, w_y, and w_z are components of h vector in UM/NAST. Therefore, the calculation of $H_{\text{jac}}(\eta)$ is performed using the following expression,

$$H_{\text{jac}}(\eta) = \sum_e H_{\text{jac}}^{(e)}(\eta), \tag{62}$$

where

$$H_{\text{jac}}^{(e)}(\eta) = \sum_{j=1}^{4} \sum_{i=1}^{4} \widetilde{h^{(e)}}(i) \, M^{(e)}(i, j) \, J_{h\eta}^{(e)}(j). \tag{63}$$

Similar techniques can be applied to the calculation of $H_{\text{hess}}(\eta)$, *i.e.*,

$$H_{\text{hess}}(\eta) = \sum_e H_{\text{hess}}^{(e)}(\eta), \tag{64}$$

where

$$H_{\text{hess}}^{(e)}(\eta) = \sum_{j=1}^{4} \sum_{i=1}^{4} \widetilde{h^{(e)}}(i) \, M^{(e)}(i, j) \, J_{h\eta\eta}^{(e)}(j). \tag{65}$$

Note that $J_{h\eta\eta}$ is a 3-dimensional tensor defined as

$$J_{h\eta\eta} = \frac{\partial J_{h\eta}}{\partial \eta}. \tag{66}$$

The calculation of $J_0(\eta)$ can be performed by exploiting the decomposition throughout the elements, *i.e.*,

$$J_0(\eta) = \sum_e J_0^{(e)}(\eta), \tag{67}$$

where

$$J_0^{(e)}(\eta) = - \int_{\Delta s} \int_{A(s)} (\tilde{r}_w + y \tilde{w}_y + z \tilde{w}_z) \left(\frac{\widetilde{\partial r_w}}{\partial \eta} + y \frac{\widetilde{\partial w_y}}{\partial \eta} + z \frac{\widetilde{\partial w_z}}{\partial \eta} \right) \rho \, dA \, ds. \tag{68}$$

11

Following the same arrangement in Eq. (61), its evaluation is given by

$$J_0^{(e)}(\eta) = -\sum_{j=1}^{4}\sum_{i=1}^{4} \widetilde{h^{(e)}}(i)\, M^{(e)}(i,j)\, \widetilde{J_{h\eta}}^{(e)}(j). \tag{69}$$

To obtain $v(\eta)$, one also relies on the decomposition across the elements, *i.e.*,

$$v(\eta) = \sum_{e} v^{(e)}(\eta), \tag{70}$$

where

$$v^{(e)}(\eta) = -\int_{\Delta s}\int_{A(s)} \left(\frac{\partial r_w}{\partial \eta} + y\frac{\partial w_y}{\partial \eta} + z\frac{\partial w_z}{\partial \eta}\right)^{\!\top}\left(\widetilde{\frac{\partial r_w}{\partial \eta}} + y\widetilde{\frac{\partial w_y}{\partial \eta}} + z\widetilde{\frac{\partial w_z}{\partial \eta}}\right)\rho\, dA\, ds. \tag{71}$$

Following the same arrangement in Eq. (61), its evaluation is given by

$$v^{(e)}(\eta) = -\sum_{j=1}^{4}\sum_{i=1}^{4} \left(J_{h\eta}{}^{(e)}(i)\right)^{\!\top} M^{(e)}(i,j)\, \widetilde{J_{h\eta}}^{(e)}(j). \tag{72}$$

This decomposition across the elements also provides a different way to calculate the center of mass $r_C(\eta)$, which is based on

$$r_C(\eta) = \sum_{e} r_C^{(e)}(\eta), \quad \frac{\partial r_C(\eta)}{\partial \eta} = \sum_{e} \frac{\partial r_C(\eta)}{\partial \eta}^{(e)}, \tag{73}$$

where

$$r_C^{(e)}(\eta) = \frac{1}{m}\int_{\Delta s}\int_{A(s)} \left(r_w + yw_y + zw_z\right)\rho\, dA\, ds = \frac{1}{m}\sum_{j=1}^{4} M^{(e)}(1,j)\, h^{(e)}(j), \tag{74}$$

$$\frac{\partial r_C(\eta)}{\partial \eta}^{(e)} = \frac{1}{m}\int_{\Delta s}\int_{A(s)} \left(\frac{\partial r_w}{\partial \eta} + y\frac{\partial w_y}{\partial \eta} + z\frac{\partial w_z}{\partial \eta}\right)\rho\, dA\, ds = \frac{1}{m}\sum_{j=1}^{4} M^{(e)}(1,j)\, J_{h\eta}^{(e)}(j). \tag{75}$$

The advantage of this formulation is that the derivative term $\frac{\partial r_C(\eta)}{\partial \eta}$ is directly calculated using the Jacobian $J_{h\eta}$ and the finite element mass matrix.

IV. Simulation Results

A. XRF1-HARW Model

The new approach of VFA low-order modeling is exemplified using a high-aspect-ratio-wing commercial transport aircraft denoted by XRF1-HARW. The XRF1 model is a representative example of current long-range wide-body commercial transport aircraft. The XRF1-HARW model has been generated based on the conventional XRF1 with an increased aspect-ratio wing but the same fuselage and tail, as shown in Figure 4. The XRF1-HARW aircraft weighs 1.29×10^5 kg, and has a wingspan of 70 m. Its modeling using UM/NAST and the comparison to the corresponding NASTRAN models are detailed in [22]. This XRF1-HARW UM/NAST is referred to as the full-order model in this paper, which contains 1085 states, including 13 rigid states and 1072 flexible strain states (*i.e.*, ϵ and $\dot{\epsilon}$).

Regarding the control effectors, the XRF1-HARW model originally had nine: two engines to produce thrust, two ailerons per wing, one elevator divided into a left and a right section, and a rudder. In this paper, the number of control inputs is reduced based on the following definitions and input grouping:

- the two engines produce equal thrust T;
- the outer ailerons are not deflected;
- the left and right elevator sections are equally deflected by an angle δ_e;
- the left and right inboard ailerons are anti-symmetrically deflected by an angle δ_a;
- the rudder is deflected by an angle δ_r.

12

Accordingly, the control surface deflection vector δ is defined as

$$\delta = \{\delta_e \quad \delta_a \quad \delta_r\}^\top. \tag{76}$$

To illustrate the strain-based mode, the displacement corresponding to a unit η_1 and η_2 are shown in Figure 5. They are out-of-plane bending modes on the left and right wings.

The out-of-plane bending curvatures at the root of the wings are chosen as examples of critical stations for monitoring the structural responses (*e.g.*, when controlling maneuver loads). They are two entries in the ϵ vector and are defined as κ_L and κ_R for left and right wing, respectively. These bending curvatures can be conveniently calculated from the new low-order models using the relationship between η and ϵ given in Eq. (51).
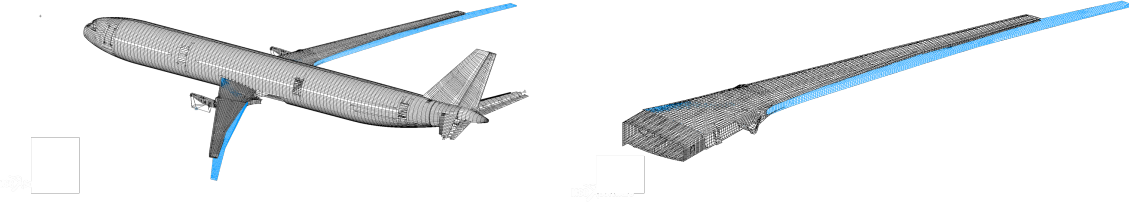
Fig. 4   Comparison of the XRF1 (black) and XRF1-HARW (blue) wing box and body [22]
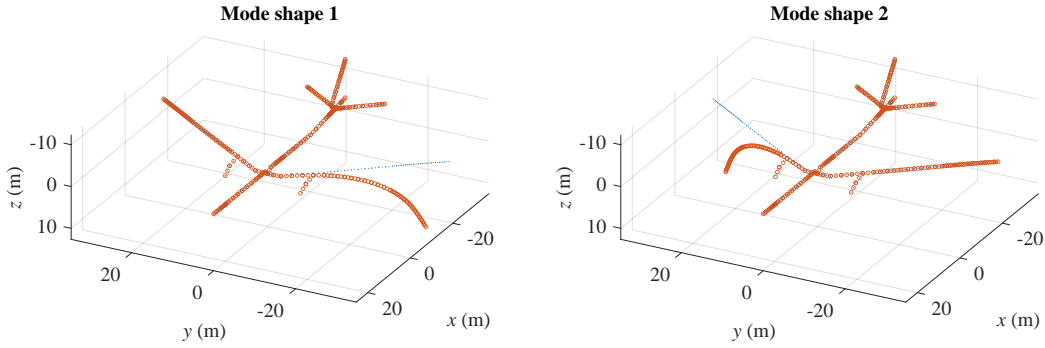
Fig. 5   XRF1-HARW deformed shape corresponding to the first two strain-based mode shapes

B. Nonlinear Function Identification

Following the procedure detailed in Section III, the nonlinear terms in Eq. (46) are represented by neural networks with a single hidden layer. Four strain-based modes are preserved in the study, and the trimmed strain state is selected to be ϵ^0 in Eq. (51). For the structural terms in Table 1, $1,000$-random η samples within the prescribed bounds are generated. With $h(\eta)$ and $J_{h\epsilon}(\eta)$ computed by UM/NAST structural solver, the output samples of the nonlinear functions in Table 1 are calculated using Eqs. (56)–(75). These samples of input-output pair are thus trained to fit the neural networks. The neural network architecture with a sufficient number of neurons has been chosen to guarantee the coefficients of determination (*i.e.*, R^2) to be larger than 0.99. Due to different dimensions of the nonlinear functions, 50 neurons are used for the approximation of $r_C(\eta), r_{T,i}(\eta), e_i(\eta), I_B(\eta), M(\eta)$ and $H_{jac}(\eta)$, while 200 neurons are used for the approximation of $J_0(\eta)$ and $v(\eta)$. The aerodynamic terms' input size is significantly larger than the structural terms, thus, $10,000$-random samples of the rigid-body state, flexible state and their rates are generated, and the corresponding aerodynamic loads are evaluated using UM/NAST static solver. The approximation of the aerodynamics also employs a neural network with a single hidden layer and 200 neurons. For all the data generated, 70% of the input/output data are used for training, 15% of the data are used for validation, while another 15% of data are used for testing. The trained result of $r_C(\eta)$ is shown with the first two strain-based modes in Figure 6. Since the first two modes are the out-of-plane bending modes, the nonlinear deformation effect on the center of mass is primarily along the z (vertical) axis and is almost linear with respect to η_1 and η_2. The nonlinear functions' dependence along of the x and y

axes, though relatively small, is still captured in the trained neural network. Note that the term $\frac{\partial r_C(\eta)}{\partial \eta}$ can either be generated from taking the analytical derivative of the fitted $r_C(\eta)$ or by fitting the data generated using Eq. (75). To test this usage of analytical derivative of the neural network, 20 random η samples are generated and the corresponding $\frac{\partial r_C(\eta)}{\partial \eta}$ is calculated using UM/NAST structure solver and Eq. (75). This is referred to as the reference data, and is compared to $\frac{\partial r_C(\eta)}{\partial \eta}$ generated from taking the analytical derivative of trained $r_C(\eta)$. The comparison results are shown in Figure 7, where the analytical derivative of trained $r_C(\eta)$ captures the responses well (with R^2 larger than 0.99). Improvements to this correlation could be obtained by increasing the training data. However, the accuracy obtained from the direct derivative of the NN approximation is adequate for the current example.
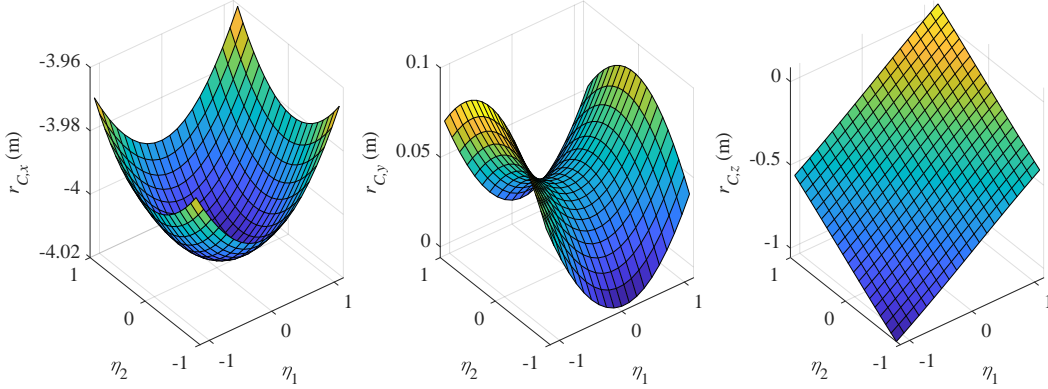
Fig. 6   Aircraft center of mass as a nonlinear function of the first two strain-based modal amplitudes
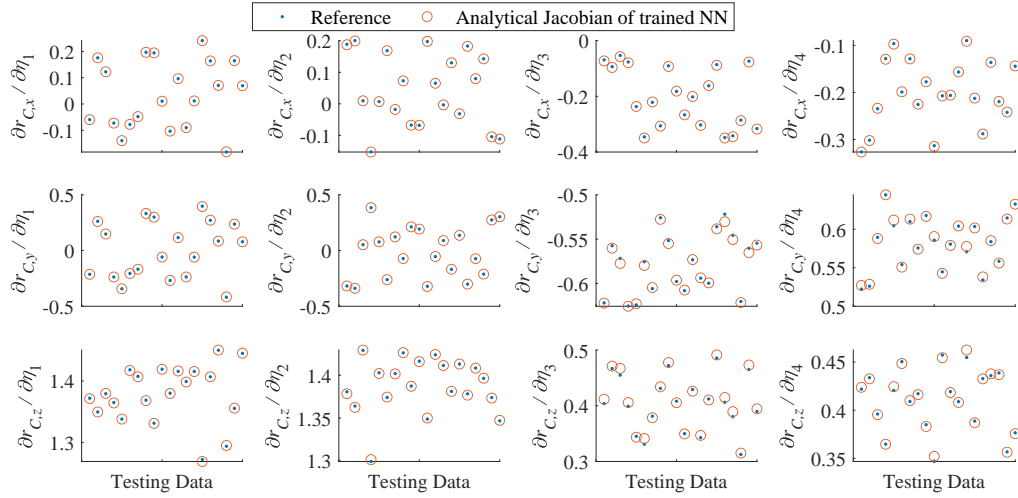

Fig. 7   Comparison of $\frac{\partial r_C(\eta)}{\partial \eta}$ generated from the analytical derivative of the neural network and the reference solution

C. Dynamic Simulation

With the trained nonlinear functions, the new VFA low-order model is employed in dynamic simulations. The XRF1-HARW is trimmed at an altitude of $8,484$ m and a speed of 254 m/s. The trimmed angle of attack is $0.5°$. Longitudinal, lateral, and coupled excitations are introduced using elevator, aileron, and rudder doublets, with the time-domain profile illustrated in Figure 8. In these doublet excitations, $t_{\text{start}} = 1$ second, $t_{\text{half}} = 4$ seconds, and $t_{\text{end}} = 7$ seconds are specified for the entire 10-second simulation. The excitation amplitudes decide the level of introduced
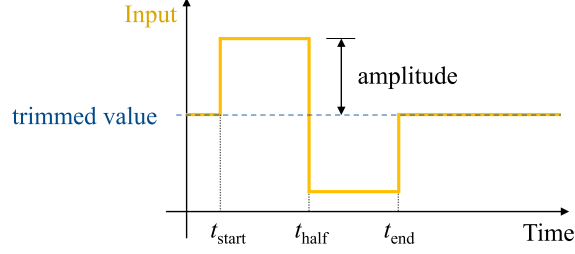
Fig. 8   Input doublet profile

geometrical nonlinearity. The left and right wing tip deflections from the full-order UM/NAST solutions under 1- and 5-degree doublet excitations, from different control surfaces and their combinations, are plotted in Figure 9 and Figure 10, respectively. Due to the North-East-Down coordinate definition, negative values of z tip displacement indicates an upwards wing shape deflection. For 1-degree elevator doublet excitation, about 4% z-tip deflections are observed during the maneuver. The 1-degree aileron and rudder doublet excitations introduce significant lower tip deflection. As shown in Figure 10, 5-degree elevator and coupled doublet excitations introduce about 23% z-tip deflections during the maneuver, where prominent geometrical nonlinearity is presented. Therefore, to showcase the new low-order model's performance, two coupled excitations (both longitudinal and lateral) of different input amplitudes representing small and large deformation are selected and simulated.
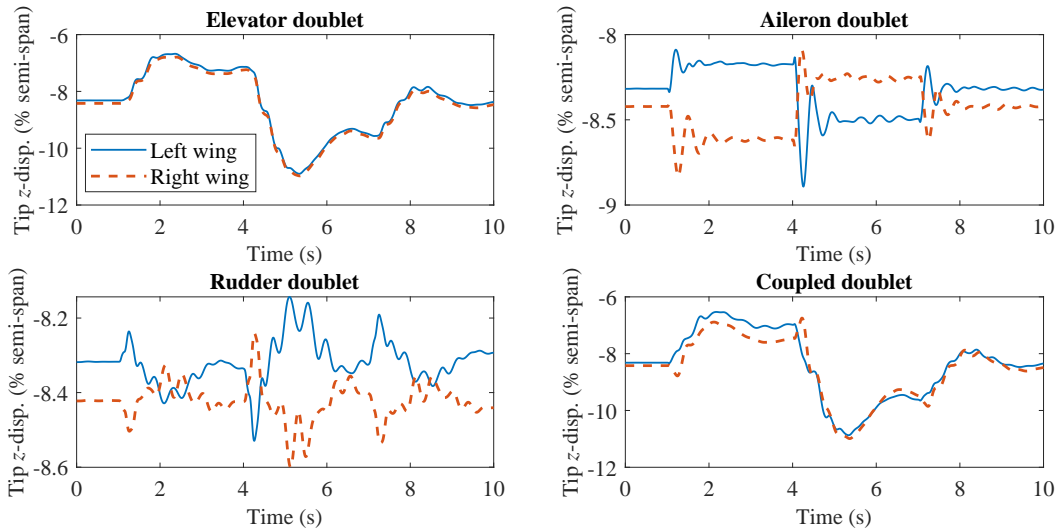

Fig. 9   Tip deflections under single-channel and coupled excitations for 1-degree doublet amplitude

The responses of the new low-order model and the full-order UM/NAST solutions under small coupled excitation (1-degree doublet input) are shown in Figures 11. The translation velocities (u, v, and w), rotation velocities (p, q, and r), Euler angles (ϕ, θ, and ψ), and representative flexible states (the out-of-plane bending curvatures at the roots of the wings (κ_L and κ_R)) are presented. The longitudinal responses of the pitch rate (q) and angle (θ) are well captured. The bending curvature trend is also captured with the new model, while the estimated amplitudes are slightly smaller than the UM/NAST solution. This arises from the discarded strain-based mode shapes, which also contribute to the responses of the rigid-body and flexible states. The trend of the lateral responses (*i.e.*, the roll rate (p), yaw rate (r), roll angle (ϕ), and yaw angle (ψ)) are also captured. High-frequency responses in the full-order UM/NAST solution are not present in the low-order model since only the first four low-frequency strain-based modes are preserved in it.

The responses of the low-order model and the full-order UM/NAST solutions under large coupled excitation (5-degree doublet input) are shown in Figures 12. The longitudinal responses of the forward speed u, the vertical speed w, the pitch rate q, and the pitch angle θ are well captured. Also, the trend of the bending curvature is also well captured with the low-order model. Note that the profiles of the responses are different compared to the small-excitation
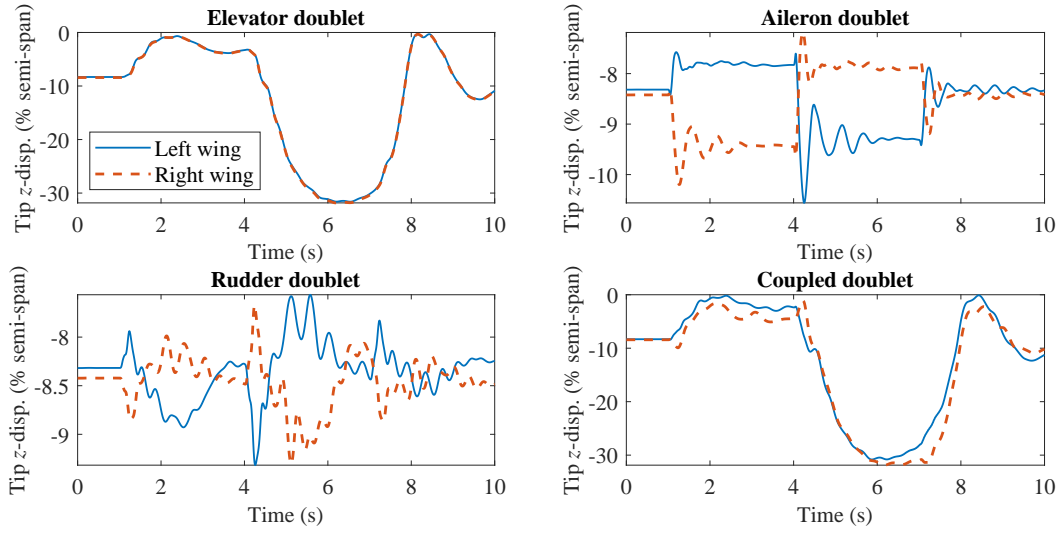
15

Fig. 10   Tip deflections under single-channel and coupled excitations for 5-degree doublet amplitude
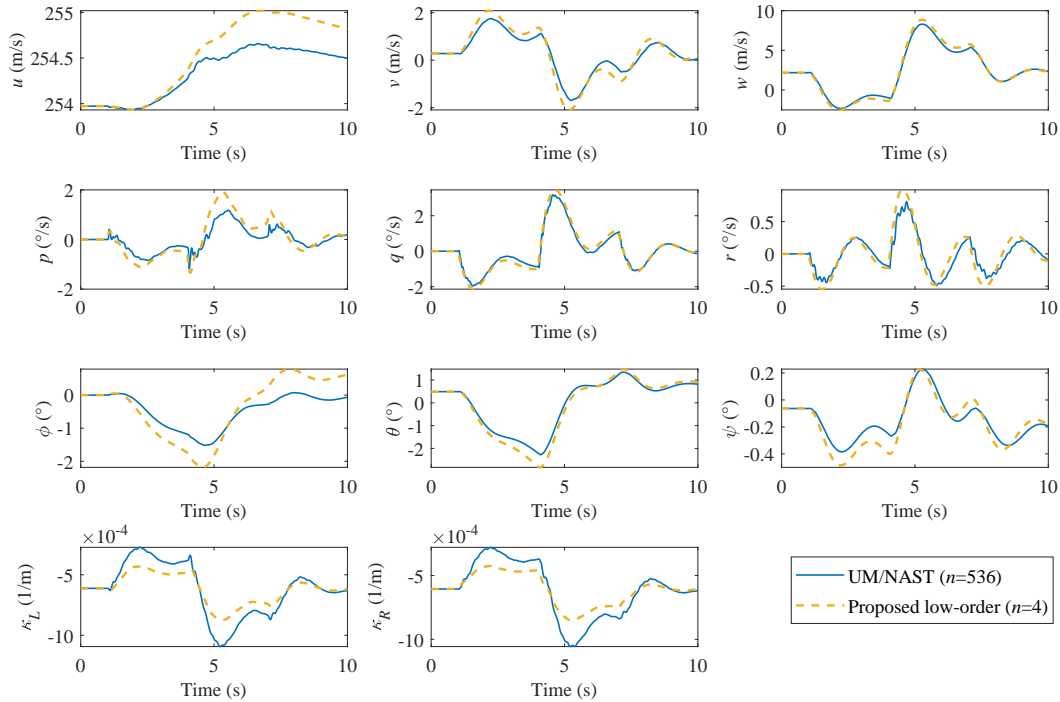

Fig. 11   Dynamic response to coupled 1-degree elevator, aileron, and rudder doublet excitation

responses shown in Figures 11, particularly around 7 seconds, where the curvature reaches its maximum absolute value. This indicates that the low-order model captures the longitudinal responses considering geometrical nonlinearities. However, the lateral responses (primarily roll rate p and yaw rate r) with a small number of flexible state ($n = 4$) exhibit a phase shift after 6 seconds. The profile of the responses is more like the responses of the small-amplitude excitations shown in Figures 11. This inaccuracy arises from two primary sources, *i.e.*, the limited number of the preserved modes
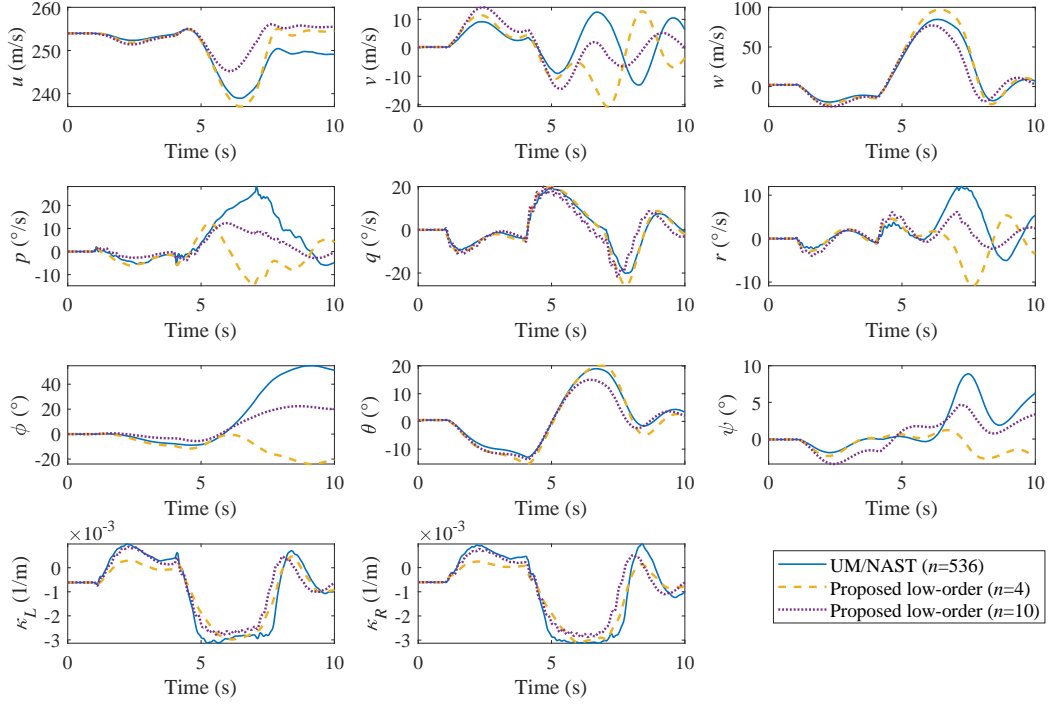
Fig. 12 Dynamic response to coupled 5-degree elevator, aileron, and rudder doublet excitation

onto which the full-order equations are projected and the inaccuracy in the neural net training of aerodynamic loads. The low-order model with an increased number of preserved modes ($n = 10$) shows an enhanced prediction of the trend in that it no longer exhibits the phase shift observed in the low-order model with $n = 4$. However, the lateral responses' error is still higher compared to the longitudinal responses due to its relatively smaller and noisier terms, which are not prioritized in the aerodynamics training. Therefore, to further enhance the lateral responses' accuracy, a more dedicated training process considering the differences in longitudinal and lateral terms needs to be established.

V. Conclusion

A modeling framework for the flight dynamics of very flexible aircraft is presented that leads to nonlinear low-order models accounting for geometric nonlinearities due to large deformations. The equations were established to represent the dynamics of the rigid-body degrees of freedom and the aeroelastic behavior of the free-flying vehicle based on a low number of strain-based modal amplitudes. The new model preserves the physical meaning of the terms in classical flight dynamics and augments it with the nonlinear elastic-related ones. The new (nonlinear) terms in the equations of motion, along with the distributed aerodynamic loads, need to be identified from the reference full-order model. A specific way of identifying these nonlinear functions was detailed here. It is based on neural network training applied to the data generated from the aircraft's full-order model using the University of Michigan's Nonlinear Aeroelastic Simulation Toolbox (UM/NAST). The new low-order modeling approach is illustrated for a high-aspect-ratio-wing commercial transport aircraft model (XRF1-HARW), representing a very flexible aircraft. As the results showed, the number of flexible states can be significantly reduced, while capturing the responses provided by the full-order model.

Appendix: Derivatives of Shallow Neural Network

The input and output of the shallow neural network are defined to be x and y. The nonlinear function is written as

$$\bar{y} = L_2 \text{tansig}(L_1 \bar{x} + b_1) + b_2, \tag{77}$$

17

where $\bar{x}$ and $\bar{y}$ are the input and output normalized by the range of the input and output data. For scalar nonlinear function, the normalization is written as

$$\bar{x} = \frac{2(x - x_{\min})}{x_{\max} - x_{\min}} + 1, \tag{78}$$

$$\bar{y} = \frac{2(y - y_{\min})}{y_{\max} - y_{\min}} + 1. \tag{79}$$

For general multi-dimensional nonlinear function, the normalization is written as

$$\bar{x} = 2\Delta_x^{-1}(x - x_{\min}) + 1, \tag{80}$$

$$\bar{y} = 2\Delta_y^{-1}(y - y_{\min}) + 1, \tag{81}$$

where

$$\Delta_x = \text{diag}\left\{x_{\max,1} - x_{\min,1}, x_{\max,2} - x_{\min,2}, ..., x_{\max,n_x} - x_{\min,n_x}\right\}, \tag{82}$$

$$\Delta_y = \text{diag}\left\{y_{\max,1} - \min,1, y_{\max,2} - y_{\min,2}, ..., y_{\max,n_y} - y_{\min,n_y}\right\}. \tag{83}$$

Function $\text{tansig}(x)$ (shown in Figure 13) is the selected activation function and is defined as

$$\text{tansig}(x) = \frac{2}{e^{-2x} + 1} - 1. \tag{84}$$

The first and second order derivatives are given by

$$\text{tansig}'(x) = \frac{d}{dx}\text{tansig}(x) = \frac{4e^{-2x}}{(e^{-2x} + 1)^2}, \tag{85}$$

$$\text{tansig}''(x) = \frac{d^2}{dx^2}\text{tansig}(x) = \frac{16e^{-4x}}{\left(e^{-2x} + 1\right)^3} - \frac{8e^{-2x}}{\left(e^{-2x} + 1\right)^2}. \tag{86}$$
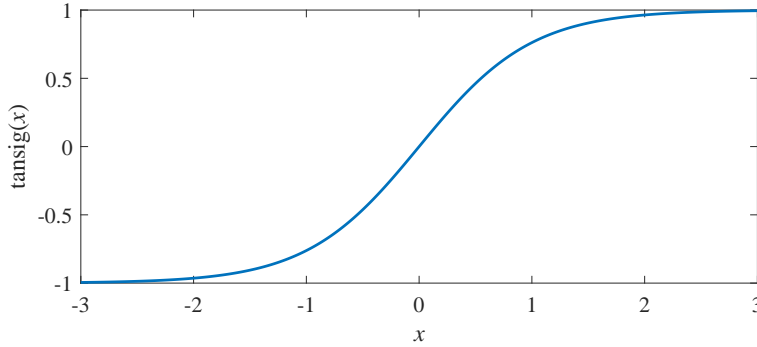

Fig. 13   Illustration of $\text{tansig}(x)$ **function**

The calculation of Jacobian of the nonlinear function is written as

$$\frac{\partial y}{\partial x} = \frac{\partial y}{\partial \bar{y}} \frac{\partial \bar{y}}{\partial \bar{x}} \frac{\partial \bar{x}}{\partial x}. \tag{87}$$

Note that

$$\frac{\partial y}{\partial \bar{y}} = \frac{\Delta_y}{2}, \quad \frac{\partial \bar{x}}{\partial x} = 2\Delta_x^{-1}. \tag{88}$$

The derivatives of the normalized input and output

$$\frac{\partial \bar{y}}{\partial \bar{x}} = L_2 \text{diag}\{\text{tansig}^{(1)}(x_{\text{NN}})\} L_1, \tag{89}$$

where
$$x_{\text{NN}} = L_1\bar{x} + b_1. \tag{90}$$

For second-order and higher-order derivatives, the tensor notation is used for clarity. Equation (77) in tensor notation is written as
$$\bar{y}_i = \sum_a L_{2,ia}\text{tansig}\left(\sum_j L_{1,aj}\bar{x}_j + b_{1,a}\right) + b_{2,i}. \tag{91}$$

The first- and second-order derivatives are given as
$$\frac{\partial y_i}{\partial x_j} = \sum_a \Delta_{y,ii}L_{2,ia}\text{tansig}'(x_{\text{NN,a}})L_{1,aj}\Delta_{x,jj}^{-1}, \tag{92}$$

$$\frac{\partial^2 y_i}{\partial x_j \partial x_k} = \sum_a \Delta_{y,ii}L_{2,ia}\text{tansig}''(x_{\text{NN,a}})L_{1,aj}L_{1,ak}\Delta_{x,jj}^{-1}\Delta_{x,kk}^{-1}. \tag{93}$$

Acknowledgments

References

[1] Shearer, C. M., and Cesnik, C. E. S., "Nonlinear flight dynamics of very flexible aircraft," *Journal of Aircraft*, Vol. 44, No. 5, 2007, pp. 1528–1545. doi:10.2514/1.27606.

[2] Su, W., and Cesnik, C. E. S., "Strain-based geometrically nonlinear beam formulation for modeling very flexible aircraft," *International Journal of Solids and Structures*, Vol. 48, No. 16-17, 2011, pp. 2349–2360.

[3] Trame, L., Williams, L., and Yurkovich, R., "Active aeroelastic oscillation control on the F/A-18 aircraft," *Guidance, Navigation and Control Conference*, 1985, p. 1858.

[4] Silvestre, F. J., Guimarães Neto, A. B., Bertolin, R. M., da Silva, R. G. A., and Paglione, P., "Aircraft control based on flexible aircraft dynamics," *Journal of Aircraft*, 2017, pp. 262–271.

[5] Schmidt, D. K., and Raney, D. L., "Modeling and simulation of flexible flight vehicles," *Journal of Guidance, Control, and Dynamics*, Vol. 24, No. 3, 2001, pp. 539–546. doi:10.2514/2.4744.

[6] Tuzcu, I., and Meirovitch, L., "Effects of flexibility on the stability of flying aircraft," *Journal of Dynamic Systems, Measurement, and Control*, Vol. 127, No. 1, 2005, pp. 41–49. doi:10.1115/1.1870040.

[7] Lanchares, M., Kolmanovsky, I., Cesnik, C. E. S., and Vetrano, F., "Model order reduction for coupled nonlinear aeroelastic-flight mechanics of very flexible aircraft," 2019.

[8] Qu, Z., and Annaswamy, A. M., "Adaptive output-feedback control with closed-loop reference models for very flexible aircraft," *Journal of Guidance, Control, and Dynamics*, Vol. 39, No. 4, 2016, pp. 873–888.

[9] Avanzini, G., Capello, E., and Piacenza, I. A., "Mixed Newtonian–Lagrangian approach for the analysis of flexible aircraft dynamics," *Journal of Aircraft*, Vol. 51, No. 5, 2014, pp. 1410–1421. doi:10.2514/1.C032235.

[10] Wang, Y., Song, H., Pant, K., Brenner, M. J., and Suh, P. M., "Model order reduction of aeroservoelastic model of flexible aircraft," *57th AIAA/ASCE/AHS/ASC Structures, Structural Dynamics, and Materials Conference*, 2016, p. 1222.

[11] Zhu, J., Wang, Y., Pant, K., Suh, P. M., and Brenner, M. J., "Genetic algorithm-based model order reduction of aeroservoelastic systems with consistent states," *Journal of aircraft*, Vol. 54, No. 4, 2017, pp. 1443–1453.

[12] Milne, R. D., *Dynamics of the deformable aeroplane*, HM Stationery Office, 1964.

[13] Canavin, J. R., and Likins, P. W., "Floating reference frames for flexible spacecraft," *Journal of Spacecraft and Rockets*, Vol. 14, No. 12, 1977, pp. 724–732. doi:10.2514/3.57256.

[14] D'Eleuterio, G. M. T., and Barfoot, T. D., "A discrete quasi-coordinate formulation for the dynamics of elastic bodies," *Journal of Applied Mechanics*, Vol. 74, No. 2, 2006, pp. 231–239. doi:10.1115/1.2189873.

[15] Gibson, T., Annaswamy, A., and Lavretsky, E., "Modeling for control of very flexible aircraft," American Institute of Aeronautics and Astronautics, 2011. doi:10.2514/6.2011-6202.

[16] Avanzini, G., Nicassio, F., and Scarselli, G., "Reduced-order short-period model of flexible aircraft," *Journal of Guidance, Control, and Dynamics*, Vol. 40, No. 8, 2017, pp. 2017–2029. doi:10.2514/1.G002387.

[17] Li, N., Grant, P., and Abbasi, H., "A comparison of the fixed-axes and the mean-axes modeling methods for flexible aircraft simulation," AIAA Guidance, Navigation, and Control and Co-located Conferences, American Institute of Aeronautics and Astronautics, 2010. doi:10.2514/6.2010-7605.

[18] Da Ronch, A., Badcock, K., Wang, Y., Wynn, A., and Palacios, R., "Nonlinear model reduction for flexible aircraft control design," *AIAA Atmospheric Flight Mechanics Conference*, 2012, p. 4404.

[19] Su, W., and Cesnik, C. E. S., "Strain-based analysis for geometrically nonlinear beams: a modal approach," *Journal of Aircraft*, Vol. 51, No. 3, 2014, pp. 890–903.

[20] Palacios, R., and Cea, A., "Nonlinear modal condensation of large finite element models: application of Hodges's intrinsic theory," *AIAA Journal*, Vol. 57, No. 10, 2019, pp. 4255–4268.

[21] Greenwood, D. T., *Advanced Dynamics*, Cambridge University Press, 2006.

[22] Riso, C., Sanghi, D., Cesnik, C. E. S., Vetrano, F., and Teufel, P., "Parametric roll maneuverability analysis of a high-aspect-ratio-wing civil transport aircraft," *AIAA Scitech 2020 Forum*, 2020, p. 1191.